

Suzaku Observation of 30 Dor C: A Supernova Remnant with the Largest Non-Thermal Shell

Hiroya YAMAGUCHI

RIKEN (The Institute of Physical and Chemical Research), 2-1 Hirosawa, Wako, Saitama 351-0198

hiroya@crab.riken.jp

Aya BAMBA

Institute of Space and Astronautical Science, JAXA, 3-1-1 Yoshinodai, Sagami-hara, Kanagawa 229-8510

and

Katsuji KOYAMA

Department of Physics, Kyoto University, Kitashirakawa-oiwake-cho, Sakyo-ku, Kyoto 606-8502

(Received 2008 June 30; accepted 2008 July 26)

Abstract

This paper reports on the Suzaku results of thermal and non-thermal features of 30 Dor C, a supernova remnant (SNR) in a superbubble of the Large Magellanic Cloud (LMC). The west rim exhibits a non-thermal X-ray spectrum with no thermal component. A single power-law model is rejected but a power-law model with spectral cutoff is accepted. The cutoff frequency of $(3 - 7) \times 10^{17}$ Hz is the highest among the shell type SNRs like SN 1006 ($\sim 6 \times 10^{16}$ Hz), and hence 30 Dor C would be the site of the highest energy accelerator of the SNR shock. The southeast (SE) and northeast (NE) rims have both the thermal and non-thermal components. The thin-thermal plasmas in the both rims are in collisional ionization equilibrium state. The electron temperature of the plasma in the SE rim ($kT_e \sim 0.7$ keV) is found to be higher than the previously reported value. The power-law index from SE is nearly the same as, while that from the NE is larger than that of the West rim. The SNR age would be in the range of $(4 - 20) \times 10^3$ yr. Thus, 30 Dor C is likely to be the oldest shell-like SNR with non-thermal emission.

Key words: ISM: individual (30 Dor C) — supernova remnants — X-Rays: spectra

1. Introduction

OB associations typically contain a few 10 massive stars. The combined actions of fast stellar winds and core-collapse supernova (SN) explosions of the member stars create large ($\gtrsim 10$ pc) shell-like structures, called superbubbles (SBs), by sweeping up the ambient medium (e.g., Mac Low & McCray 1988). Therefore, SBs are very energetic objects which store a large amount of energy injected from massive stars; the swept up interstellar medium (ISM) can be successively heated to high temperature by stellar winds and/or SNe. Furthermore, large tenuous cavities created inside the SB walls allow that the blast shocks of the interior supernova remnants (SNRs) expand rapidly without decelerating for a long time. Therefore, the timescale of efficient cosmic-ray acceleration can be much longer than that of most isolated SNRs.

For the study of SNRs and SBs, the Large Magellanic Cloud (LMC) is an ideal site, because of little foreground extinction and well-known distance (50 kpc: Alves 2004). Dunne, Points, Chu (2001) systematically studied several SBs in the LMC using ROSAT, and showed their X-ray emissions are brighter than that theoretically expected for a wind-blown bubble. This fact suggests that the X-ray emitting walls of the SBs are re-heated by the shock of interior SNRs, and hence the emissions are enhanced. They also found that the plasma temperatures of the shocked

SB walls are typically of the order of 0.1 keV.

30 Dor C, located in the southwestern region of the 30 Doradus complex, is one of the SBs in the LMC identified by the morphology of the $H\alpha$ emission (Mathewson et al. 1985; Kennicutt & Hodge 1986). This SB hosts an OB association LH 90, with the age of a few Myr (Lucke & Hodge 1970). A shell-like structure with a diameter of $\sim 6'$ (~ 87 pc at 50 kpc distance) was discovered by the radio observation (Mills et al. 1984).

X-rays from 30 Dor C were first detected with the Einstein satellite (Long et al. 1981). Then, Dunne, Points, Chu (2001) found a clear shell-like structure confined within the $H\alpha$ shell by the ROSAT observation. They thus concluded that the X-ray emission arises from the interaction between the SB and an interior SNR. Bamba et al. (2004: hereafter B04) discovered synchrotron X-rays from the shell region of 30 Dor C with Chandra and XMM-Newton. They found that the total luminosity of the synchrotron emission was ~ 10 times larger than that of SN 1006 (Koyama et al. 1995), and hence argued that the large energy supply was probably by multiple SN explosions.

This paper reports the X-ray observation of 30 Dor C with Suzaku (Mitsuda et al. 2007). Utilizing the good sensitivity of Suzaku, we study the detailed properties of the thermal and non-thermal emissions from 30 Dor C. The distance to the LMC is assumed to be 50 kpc, following Alves (2004).

2. Observations and Data Reduction

Suzaku observed SN 1987A on 2005 November 3 (Observation ID = 500006010; hereafter Obs. 1) and on 2006 June 8 (Observation ID = 801090010; hereafter Obs. 2). In both of the observations, the 30 Dor C region was in the field of view (FOV) of X-ray Imaging Spectrometer (XIS; Koyama et al. 2007). This paper concentrates on the imaging and spectral features of 30 Dor C obtained with the XIS. The results of SN 1987A will be reported in separate paper.

Three of the XIS are front-illuminated (FI) CCDs and the remaining one is a back-illuminated (BI) CCD. The former have high sensitivity and low background for diffuse sources in the hard X-ray band of $\sim 5\text{--}10$ keV, while the latter has high sensitivity in the soft X-ray band below 1 keV. All the CCDs are placed on the foci of the X-Ray Telescopes (XRT; Serlemitsos et al. 2007) which co-aligned to image the same region of the sky. A half-power diameter (HPD) of the XRT is $\sim 1'.8 - 2'.3$, independent of the X-ray energy.

The XIS was operated in the normal full-frame clocking mode during both of the observations. We employed cleaned revision 2.0 data, which includes column-to-column correction of the charge transfer inefficiency (CTI) measured using the charge-injection (CI) capability (Nakajima et al. 2008). We used the HEADAS software version 6.4 for the data reduction and analysis. After the screening, the exposure times were obtained to be ~ 37 ks and ~ 40 ks for Obs. 1 and Obs. 2, respectively.

The errors quoted in the text and tables are at the 90% confidence level, and the 1σ confidence in the figures, unless otherwise stated.

3. XIS Image

Figure 1 shows the three-color XIS image: red, green, and blue represent 0.6–1.0 keV, 1.0–2.0 keV, and 2.0–5.0 keV, respectively. The XIS astrometry was fine-tuned using SN 1987A at (RA, Dec) = ($05^{\text{h}}35^{\text{m}}28^{\text{s}}$, $-69^{\circ}16'12''$). After the tuning, we excluded the circular region with the radius of $2'.5$ around SN 1987A to emphasize dim diffuse structures.

A clear shell-like structure of 30 Dor C can be seen at the northeast part of the FOV. The west side of the shell is bright in the hard X-ray band, whereas the eastern half is dominated by the soft X-rays below 2 keV.

In addition, we can see extended soft X-ray emission from the entire FOV, with different surface brightness from position to position.

4. Spectral Analysis

For a spatially resolved X-ray spectroscopy of 30 Dor C, we selected typical source regions and candidates of a background region. To increase statistics, the data obtained in Obs. 1 and Obs. 2 were merged both for the source and background spectra.

The selected 30 Dor C regions are shown with the three

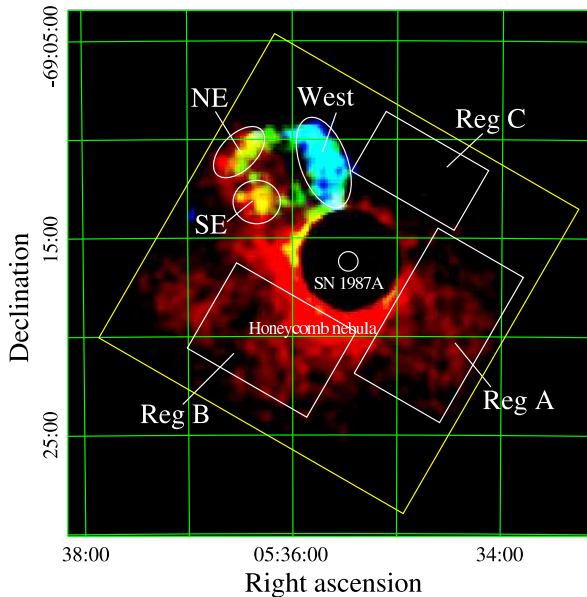


Fig. 1. Three-color XIS image around SN 1987A and 30 Dor C smoothed with a Gaussian kernel of $\sigma = 25''$. Red, green, and blue contain emissions from 0.6–1.0 keV, 1.0–2.0 keV, and 2.0–5.0 keV, respectively. The coordinates (RA and Dec) refer to epoch J2000.0. The Field of view of the XIS is indicated by the yellow square, where the data from the four XIS are combined, but that of the four corners, irradiated by the ^{55}Fe calibration sources, are removed. The ellipses and rectangles indicate the regions used in our spectral analysis (section 4). The small circle represents the position of SN 1987A, but the $2'.5$ -radius circular region around SN 1987A is excluded (see text).

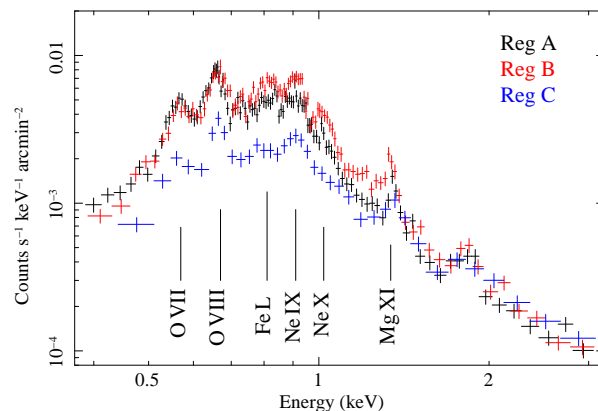


Fig. 2. XIS-BI spectra of Regions A (black), B (red) and C (blue), normalized by each solid angle. Characteristic emission lines are labeled in the panel.

ellipses in figure 1, the West, southeast (SE), and northeast (NE) regions. West was chosen as the brightest hard X-ray (2.0–5.0 keV) region, while the other two were selected from the peaks of the soft X-ray band (0.6–1.0 keV).

4.1. Background Selection and Analysis Procedure

For a proper background subtraction, we examined the spectra of source-free regions shown by rectangles

(Region A, B, and C) in figure 1. Figure 2 shows the XIS-BI spectra of these regions normalized by each solid angle. Although the spectral shapes above ~ 1.5 keV are very similar among the three rectangular regions (Region A, B, and C), the 0.4–1.0 keV surface brightness of Region C is lower, while the 0.7–1.5 keV flux of Region B is higher than those of the others.

Since a dense molecular cloud is located at the north region of our FOV (the NANTEN CO observation: Yamaguchi et al. 2001), the low energy (0.4–1.0 keV) deficiency in Region C would be due to the local interstellar absorption in the LMC.

The excess in 0.7–1.5 keV of Region B spectrum is particularly clear at the energies of the K-shell emission lines of Ne IX, Ne X, and Mg XI, and Fe L-shell blends. These features are likely to originate from thermal emissions from the Honeycomb nebula (SNR 0536–69.3: Dennerl et al. 2001), which is partially included in the Region B area, although no clear structure is found in figure 1.

We thus assumed that Region A represents a proper local background for 30 Dor C. However, the local absorption may be variable from position to position, and hence we applied the spectra analysis as follows.

(1) Non X-ray background (NXB) was constructed from the data base of night-Earth by sorting with the geomagnetic cut-off rigidity (COR) from the same region on the detector coordinates of our observation (see Tawa et al. 2008). The NXB with the same COR distribution as that of the 30 Dor C observations were subtracted from the spectra of Region A, and the West, SE, and NE regions.

(2) The NXB-subtracted spectrum of Region A was fitted with a model of the cosmic X-ray background (CXB) plus several thermal plasma components. The best-fit spectrum was used as a local background for the source spectra (West, SE, and NE).

(3) Since the source spectra include a local background, we performed model fit, by adding the Region A components and fixing the parameters other than absorptions to those of the best-fit results obtained in the process (2).

For the spectral fittings, we used the XSPEC software version 11.3.2. The data from the three XIS-FIs were merged to improve the photon statistics, since their responses are nearly identical. For simplicity, the XIS-BI spectra are not shown in figures, although they were analyzed simultaneously with the FI spectra.

4.2. Background Region (Region A)

Figure 3 shows the 0.4–10 keV spectrum of Region A. We can see many emission lines below ~ 2 keV, while the spectrum above ~ 2 keV is featureless. Therefore, we fitted the spectrum with a model of a thin-thermal plasma plus a power-law component. For the thermal plasma, we used a VAPEC model (Smith et al. 2001), allowing the electron temperature (kT_e) and emission measure (EM) to vary freely. The elemental abundances relative to solar values (Anders & Grevesse 1989) of O, Ne, Mg, Si, and Fe were also treated as free parameters, whereas those of the other elements were fixed to the mean LMC values of

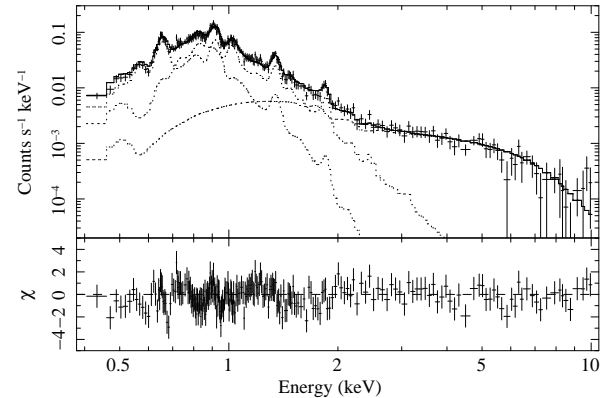


Fig. 3. XIS-FI spectrum of Region A. The non X-ray background was subtracted. The components of the best-fit model are shown with the dotted lines.

Table 1. Best-fit spectral parameters of Region A.

| Component | Parameter | Value |
|------------------------|---|--|
| Absorption* | $N_{\text{H}}^{\text{LMC}}$ (cm^{-2}) | $5.3 (0.9\text{--}9.6) \times 10^{20}$ |
| Power-law [†] | Γ | 1.412 (fixed) |
| | Norm [‡] | $3.7 (3.5\text{--}4.0) \times 10^{-5}$ |
| VAPEC | kT_{e1} (keV) [§] | 0.22 (0.21–0.24) |
| | EM_1 (cm^{-3}) ^{§#} | $5.9 (3.8\text{--}8.7) \times 10^{58}$ |
| | kT_{e2} (keV) | 0.53 (0.48–0.56) |
| | EM_2 (cm^{-3}) [#] | $2.0 (1.5\text{--}2.6) \times 10^{58}$ |
| | O (solar) | 0.30 (0.23–0.41) |
| | Ne (solar) | 0.61 (0.47–0.77) |
| | Mg (solar) | 0.53 (0.41–0.72) |
| | Si (solar) | 0.50 (0.37–0.66) |
| | Fe (solar) | 0.23 (0.19–0.30) |
| $\chi^2/\text{d.o.f.}$ | | 427/417 = 1.02 |

* Absorption in the LMC (see text).

[†] Cosmic X-ray background is assumed.

[‡] Unit is photons $\text{s}^{-1} \text{cm}^{-2} \text{keV}^{-1}$ at 1 keV.

[§] Low temperature component.

^{||} High temperature component.

[#] Emission measure ($\text{EM} = n_p n_e V$), where n_p , n_e , and V are the proton and electron densities and the plasma volume, respectively.

Russell & Dopita (1992).

Since the power-law component is mainly due to the CXB, we fixed the photon index to be $\Gamma = 1.412$, which was reported by Kushino et al. (2002). The interstellar absorption columns in the Galaxy and LMC were separately treated. The Galactic absorption column density was fixed to be $N_{\text{H}}^{\text{G}} = 6.35 \times 10^{20} \text{cm}^{-2}$ (Dickey & Lockman 1990), assuming the solar abundances. [Although the Galactic HI column densities were newly measured by Leiden/Argentine/Bonn survey (Kalberla et al. 2005), their database does not exclude the contribution of HI in the LMC.¹ Therefore, we did not use this new database.]

¹ see <http://heasarc.gsfc.nasa.gov/Tools/w3nh_help.html>, for details.

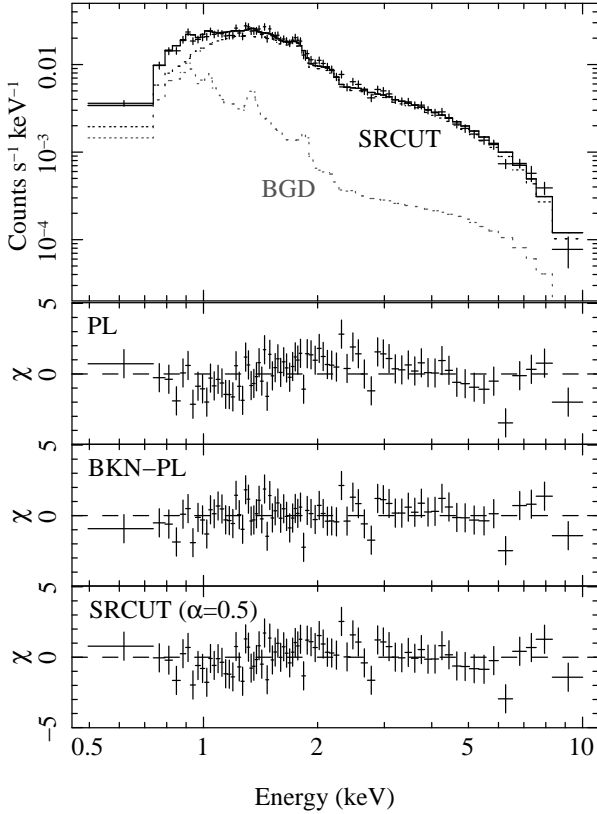


Fig. 4. Non X-ray background subtracted XIS-FI spectrum of the West rim. In the top panel, the best-fit SRCUT model is shown with the black dotted line, while the local background component is represented by the gray dotted line. The second, third, and fourth panels display the residuals from the best-fits of the power-law (PL), broken power-law (BKN-PL), and SRCUT ($\alpha = 0.5$) models, respectively.

The absorption in the LMC ($N_{\text{H}}^{\text{LMC}}$) with the LMC abundances (Russell & Dopita 1992) was treated as a free parameter.

This 2-component model gave the best-fit kT_e of 0.29 keV, while a significant data excess at the energy of the O VII $K\alpha$ line (~ 0.57 keV) are found. In fact, this model was rejected with $\chi^2/\text{d.o.f.}$ of 628/419. We hence added another thermal component with a different temperature. The metal abundances were common for both components. Then, the fit was greatly improved with $\chi^2/\text{d.o.f.}$ of 427/417. The best-fit parameters and models are respectively shown in table 1, and figure 3 with dotted lines. The 2–10 keV surface brightness of the power-law component was obtained to be 6.6×10^{-8} erg cm $^{-2}$ s $^{-1}$ sr $^{-1}$, which is consistent with being the CXB (Kushino et al. 2002).

4.3. West Rim

Figure 4 shows the spectrum of the 30 Dor C West region. Since the spectrum is featureless with no emission line, we first fitted with a power-law (PL) model plus the local background derived in subsection 4.2. Then, the obtained $\chi^2/\text{d.o.f.}$ was 191/148, hence a simple PL model is rejected. It shows the residuals with wavy shape around

Table 2. Best-fit parameters for the West spectrum.

| Parameter | Value |
|---|--|
| Power-law (PL) | |
| $N_{\text{H}}^{\text{LMC}}$ (cm $^{-2}$)* | $5.9 (5.6\text{--}6.2) \times 10^{21}$ |
| Γ | 2.17 (2.12–2.21) |
| Norm † | $2.8 (2.7\text{--}2.9) \times 10^{-4}$ |
| F_{X} (ergs s $^{-1}$ cm $^{-2}$) ‡ | 1.2×10^{-12} |
| $\chi^2/\text{d.o.f.}$ | 191/148 = 1.29 |
| Broken power-law (BKN-PL) | |
| $N_{\text{H}}^{\text{LMC}}$ (cm $^{-2}$)* | $4.4 (4.2\text{--}5.1) \times 10^{21}$ |
| Γ_1 | 1.48 (1.31–1.82) |
| Break E (keV) | 1.9 (1.7–2.5) |
| Γ_2 | 2.33 (2.26–2.50) |
| Norm † | $2.0 (1.9\text{--}2.3) \times 10^{-4}$ |
| F_{X} (ergs s $^{-1}$ cm $^{-2}$) ‡ | 9.9×10^{-13} |
| $\chi^2/\text{d.o.f.}$ | 140/146 = 0.96 |
| SRCUT ($\alpha = 0.50$) | |
| $N_{\text{H}}^{\text{LMC}}$ (cm $^{-2}$)* | $5.5 (5.2\text{--}5.7) \times 10^{21}$ |
| ν_{rolloff} (Hz) | $3.7 (3.2\text{--}4.5) \times 10^{17}$ |
| Norm § | $8.0 (7.0\text{--}9.0) \times 10^{-3}$ |
| $\chi^2/\text{d.o.f.}$ | 164/148 = 1.11 |
| SRCUT ($\alpha = 0.55$) | |
| $N_{\text{H}}^{\text{LMC}}$ (cm $^{-2}$)* | $5.5 (5.2\text{--}5.8) \times 10^{21}$ |
| ν_{rolloff} (Hz) | $4.6 (3.8\text{--}5.6) \times 10^{17}$ |
| Norm § | $1.9 (1.7\text{--}2.1) \times 10^{-2}$ |
| $\chi^2/\text{d.o.f.}$ | 166/148 = 1.12 |
| SRCUT ($\alpha = 0.60$) | |
| $N_{\text{H}}^{\text{LMC}}$ (cm $^{-2}$)* | $5.5 (5.3\text{--}5.8) \times 10^{21}$ |
| ν_{rolloff} (Hz) | $5.7 (4.7\text{--}7.1) \times 10^{17}$ |
| Norm § | $4.6 (4.1\text{--}5.2) \times 10^{-2}$ |
| $\chi^2/\text{d.o.f.}$ | 167/148 = 1.13 |

* Absorption in the LMC.

† Unit is photons s $^{-1}$ cm $^{-2}$ keV $^{-1}$ at 1 keV.

‡ Unabsorbed flux in 0.5–10 keV band.

§ Flux density at 1 GHz (Jy).

the best-fit power-law of photon index $\Gamma \sim 2.2$, as is shown in the second panel of figure 4.

We therefore, introduced a broken power-law (BKN-PL) model. Then, the $\chi^2/\text{d.o.f.}$ was significantly reduced to 140/146 to become an acceptable fit. The residual is shown in the third panel of figure 4; the wavy pattern is largely reduced. The photon indices of the BKN-PL model were respectively $\Gamma_1 \sim 1.5$ and $\Gamma_2 \sim 2.3$, below and above a break energy at ~ 1.9 keV.

We also fitted the spectrum with a more physical model, the SRCUT model (Reynolds 1998), which represents the synchrotron spectrum from electrons with an exponentially cut-off power-law energy distribution. We fixed the spectral index at 1 GHz to a typical value for SNRs of $\alpha = 0.50$. This model was also acceptable with $\chi^2/\text{d.o.f.} = 164/148$, although the residual pattern (the fourth panel of figure 4) was not removed completely. We further tried the SRCUT model for the radio indices of $\alpha = 0.55$ and 0.60. Both of the cases gave almost the same result as the $\alpha = 0.5$ model. The best-fit parameters of each model

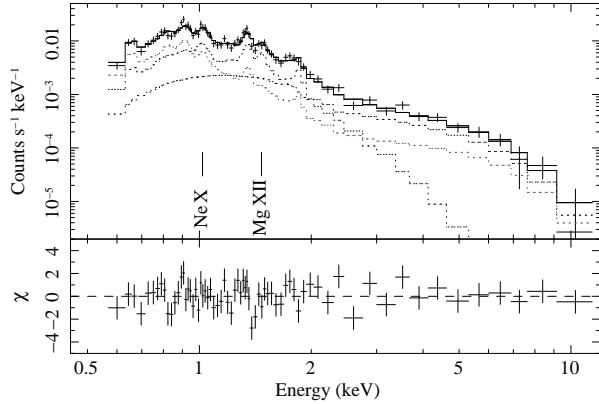


Fig. 5. Same as figure 4, but for the SE rim. The components of the best-fit model are shown with the black dotted lines. The gray dotted line represents the local background component. The energies of the emission lines from Ne X and Mg XII are indicated in the panel.

which we used here are given in table 2.

4.4. SE Rim

The spectrum of the SE region is shown in figure 5. We can see the relatively strong emission lines below ~ 2.0 keV, which suggests that the soft X-rays dominantly comes from an optically thin-thermal plasma. Indeed, B04 showed that the Chandra and XMM-Newton spectra of this region were well-reproduced by the model of the thin-thermal plasma at a collisional ionization equilibrium (CIE) plus the power-law component. Therefore, we fitted our spectrum using a VAPEC model (for the soft component), a power-law (for the hard component), and the local background. We allowed the abundances of Ne, Mg, Si, and Fe to be free. The abundance of Ni was fixed to that of Fe. Then, the fit was acceptable with $\chi^2/\text{d.o.f.}$ of 102/101. The best-fit parameters and models are shown in table 3 and figure 5, respectively.

Since the error region of the photon index (Γ) includes the best-fit value of the West rim, we fitted with the same model but fixing Γ to be 2.17, then the best-fit result were almost the same as the case of free parameter of Γ . Although we tried to fit the spectrum using a non-equilibrium ionization (NEI) plasma model instead of the VAPEC model, the fit did not improve significantly.

4.5. NE Rim

The spectrum of NE rim is shown in figure 6. Since B04 reported that no significant thermal component was detected from this region, we first fitted the spectrum with a power-law and the local background. However, this model was rejected with a $\chi^2/\text{d.o.f.}$ of 166/122. The large residuals were found at the energy of the Ne IX $K\alpha$ line (~ 0.91 keV). This fact suggests the presence of a thermal component in the soft X-ray band. Therefore, we added a VAPEC model on the power-law. The free parameters of the VAPEC component were the same as described in subsection 4.4. Then the fit was significantly improved

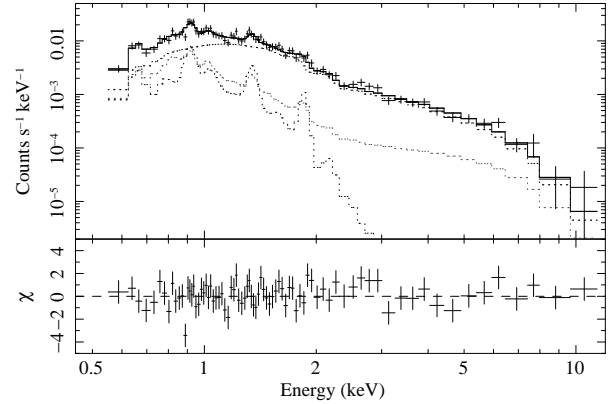


Fig. 6. Same as figure 5, but for the NE rim.

with $\chi^2/\text{d.o.f.}$ of 120/116. The best-fit parameters and models are respectively given in table 3 and figure 6.

For the NE rim, if we fitted with the same model of fixed $\Gamma = 2.17$ as the case of the SE rim, then the fit was rejected with $\chi^2/\text{d.o.f.}$ of 142/117. Thus, unlike the SE rim, the NE rim has a steeper (softer) photon index than the West. We also tried an NEI model, but no improvement of $\chi^2/\text{d.o.f.}$ value was obtained.

5. Discussion

5.1. Thermal Emission

The thermal component of the SE spectrum was well represented by the CIE plasma model with the electron temperature of ~ 0.7 keV. Since the bright $H\alpha$ emission coincides with the SE rim (Mathewson et al. 1985), the origin of the thermal component is considered to be the SB shell re-shocked by the blast-wave of the interior SNR. In addition, we detected the significant thin-thermal component from the NE rim, for the first time. This region is also correlated with the $H\alpha$ emission, albeit the brightness is lower than that of the SE region. Therefore, the same origin with the SE can be considered. The low elemental abundance of Fe relatively to the other lighter elements is probably due to that the SB shell is dominantly contributed by stellar winds and core-collapse SNRs occurred in the past.

The size of the SE elliptic region is $1/2 \times 1/1$, which corresponds to $18 \text{ pc} \times 16 \text{ pc}$ at a distance of 50 kpc. Assuming the plasma depth to be 22 pc, a half radius of the SNR, the emission volume is estimated to be $V = 5.7 \times 10^{59} \text{ cm}^3$. Thus, the EM of the VAPEC component in the SE region corresponds to the proton and electron densities of $n_p \simeq n_e = 0.37 f_{\text{SE}}^{-0.5} \text{ cm}^{-3}$, where f_{SE} is the filling factor. The plasma mass is, therefore, estimated to be $M = 175 f_{\text{SE}}^{0.5} M_{\odot}$. Similarly, from the size of the NE ellipse of $1/9 \times 0/9$, the plasma densities and the mass are respectively estimated to be $n_p \simeq n_e = 0.12 f_{\text{NE}}^{-0.5} \text{ cm}^{-3}$ and $M = 57 f_{\text{NE}}^{0.5} M_{\odot}$, where f_{NE} is the filling factor for the VAPEC component in the NE region.

Both the SE and NE plasmas were found to be in CIE condition. For full ionization equilibrium, the ionization

Table 3. Best-fit parameters of for the SE and NE spectra.

| Component | Parameter | SE | NE |
|------------------------|---|--|--|
| Absorption* | $N_{\text{H}}^{\text{LMC}}$ (cm^{-2}) | $6.2 (2.8\text{--}9.7) \times 10^{20}$ | $3.1 (2.4\text{--}4.8) \times 10^{21}$ |
| Power-law | Γ | 2.01 (1.39–2.45) | 2.56 (2.45–2.71) |
| | Norm [†] | $2.0 (0.7\text{--}3.8) \times 10^{-5}$ | $1.2 (1.1\text{--}1.5) \times 10^{-4}$ |
| VAPEC | F_{X} ($\text{ergs s}^{-1} \text{cm}^{-2}$) [‡] | 9.3×10^{-14} | 4.2×10^{-13} |
| | kT_e (keV) | 0.66 (0.58–0.76) | 0.28 (0.20–0.34) |
| | EM (cm^{-3}) [§] | $7.8 (3.2\text{--}12) \times 10^{58}$ | $9.2 (3.7\text{--}31) \times 10^{57}$ |
| | Ne (solar) | 0.33 (0.17–0.88) | 0.53 (0.30–1.1) |
| | Mg (solar) | 0.63 (0.38–1.6) | 1.1 (0.43–4.0) |
| | Si (solar) | 0.36 (0.19–0.96) | 3.0 (>0.70) |
| | Fe, Ni (solar) | 0.03 (0.01–0.08) | (<0.2) |
| $\chi^2/\text{d.o.f.}$ | | 102/101 = 1.01 | 120/116 = 1.04 |

* Absorption in the LMC.

† Unit is photons $\text{s}^{-1} \text{cm}^{-2} \text{keV}^{-1}$ at 1 keV.

‡ Unabsorbed flux in 0.5–10 keV band.

§ Emission measure ($\text{EM} = n_p n_e V$), where n_p , n_e , and V are the proton and electron densities and the plasma volume, respectively.

timescale defined as $n_e t$ is required to be $\geq 10^{12} \text{cm}^{-3} \text{s}$, where t is the plasma age or the time since the gas was shock-heated (Masai 1984). Therefore, the plasma ages of the SE and NE plasmas are estimated to be higher than $\sim 9 \times 10^4$ yr and $\sim 3 \times 10^5$ yr, respectively. As mentioned in subsection 5.2, the real age of the SNR is likely to be lower than $\sim 2 \times 10^4$ yr. Thus, the plasma ages are significantly older than the SNR age. This fact can be interpreted that the SB shell had been ionized by preceding stellar winds and/or SNe, before the re-heating by the interior SNR. In CIE plasma, energy equipartition between electron and protons can be assumed. Therefore, the thermal energies ($E = 3n_e V kT_e$) of the SE and NE plasmas are estimated to be 6.7×10^{50} ergs and 1.2×10^{50} ergs, respectively.

The electron temperature derived for the SE rim (0.58–0.76 keV) is significantly higher than the value of the previous report of B04 (0.19–0.23 keV). If we fitted the SE spectrum fixing the temperature to 0.21 keV, the best-fit value of B04, the model failed to reproduce the fluxes of the Ne X and Mg XII $K\alpha$ lines, which are clearly detected in our spectrum (see figure 5). Indeed, the $K\alpha$ -line flux ratios of Ne X/Ne IX and Mg XII/Mg XI predicted by the 0.21 keV CIE plasma are only less than 10%. Since the emission lines from these hydrogen-like ions were not detected in the Chandra spectrum probably due to the poor photon statistics and relatively poor energy resolution, the systematically lower temperature would be obtained by B04.

5.2. Non-Thermal Emission

The high quality spectrum of the West rim rejected the simple power-law model. We found that either the broken power-law or the SRCUT was required to fit the West spectrum, for the first time. Similar spectral steepening had been found in the synchrotron X-rays from the other SNRs, SN 1006 (Bamba et al. 2008) and RX J1713.7–3946 (Takahashi et al. 2008). Therefore, the previous argument (B04) becomes more robust that the non-thermal X-rays

from 30 Dor C are synchrotron emissions from high energy electrons accelerated by the shock front of the SNR.

In the SRCUT model for the West rim, the roll-off frequency was obtained to be $(3\text{--}7) \times 10^{17}$ Hz for the typical range of the spectral index at the radio band of $\alpha = 0.5\text{--}0.6$. We also tried to fit the SE and NE spectra using the SRCUT models with $\alpha = 0.5$ instead of the power-law components. Then, the roll-off frequencies were obtained to be $> 1.1 \times 10^{17}$ Hz and $(0.7\text{--}1.4) \times 10^{17}$ Hz, respectively. All these values are significantly higher than that of SN 1006 ($\sim 6 \times 10^{16}$ Hz: Bamba et al. 2008), and similar to RX J1713.7–3946 ($\sim 2 \times 10^{17}$ Hz: Takahashi et al. 2008), the highest value among the shell-like SNRs. Since $\nu_{\text{rolloff}} \propto B E_e^2$, where B and E_e are the magnetic field and the maximum energy of accelerated electrons (Reynolds 1998), the electrons would be accelerated to higher energy than that in the case of SN 1006, if the comparable strengths of the magnetic field are assumed.

30 Dor C has a radius of ~ 44 pc, which is much larger than any other shell-like SNRs with non-thermal emission (e.g., RX J1713.7–3946, RX J0852.0–4622, RCW 86: $r < 20$ pc). If we simply assume that the blast-wave have been expanded almost freely in the cavity with the initial speed (possibly $\sim 10^4 \text{km s}^{-1}$), then the SNR age would be $\sim 4 \times 10^3$ yr. These may be the lower limit of the age. On the other hand, in order to emit intense synchrotron X-rays, the shock speed higher than $\sim 2000 \text{km s}^{-1}$ is required by the standard diffusive shock acceleration theory (e.g., Aharonian & Atoyan 1999). Therefore, the upper limit of the age is estimated to be $\sim 2 \times 10^4$ yr. We thus conclude that the age of 30 Dor C would be between $\sim 4 \times 10^3$ yr and $\sim 2 \times 10^4$ yr; 30 Dor C is the oldest among the known non-thermal SNRs.

Our observation demonstrates even older-system can be a site of higher energy acceleration than typical young SNRs, such as SN 1006. RCW 86 is another shell-like SNR with non-thermal shell, which has a relatively old age of ~ 1800 yr. Similarly to 30 Dor C, RCW 86 also co-

incides with the OB association, and is considered to be fast expanding inside the large cavity (Vink et al. 2006; Yamaguchi et al. 2008). The long timescales of the efficient acceleration, achieved in 30 Dor C and RCW 86, would be due to the extremely low density of the cavity created inside the SB shell; the SNRs in SBs can be better cosmic-ray accelerator than the isolated SNRs in homogeneous ISM.

Non-thermal X-rays had been detected from other star-forming regions, RCW 38 (Wolk et al. 2002) and Westerlund 1 (Muno et al. 2006) in our Galaxy, and DEM L192 (N51D: Cooper et al. 2004) in the LMC. However, the emissions from these regions show center-filled morphologies, in contrast to those from 30 Dor C and RCW 86. Moreover, their photon indexes (e.g., $\Gamma \sim 1.3$ for DEM L192) are lower (harder) than those of typical shell-like SNRs. Therefore, the origins of these emissions are still unclear. Future detailed studies of the thermal and non-thermal properties of these star-forming regions using sensitive observatory, such as Suzaku, would help to reveal their origins. Observations of more SBs are also necessary to determine if non-thermal emissions are commonly present or not in SB regions.

6. Summary

We have analyzed Suzaku/XIS data of 30 Dor C. The results are summarized as follows:

1. The West rim is dominated by the non-thermal emission, whereas the SE and NE rims show the thermal and non-thermal emissions.
2. The spectrum from the West rim is well-reproduced by a power-law with spectral cutoff. The cutoff frequency of $(3 - 7) \times 10^{17}$ Hz is the highest, although the age is the oldest, among the known shell-like SNRs with non-thermal emission.
3. The thermal components of the SE and NE spectra are well-represented by the plasma at a collisional ionization equilibrium.
4. The electron temperature of the thermal plasma in the SE rim ($kT_e \sim 0.7$ keV) is found to be higher than the value of the previous report.

The authors would like to thank the Suzaku Science Working Group and the members of Suzaku SN 1987A team. We also thank Yasunobu Uchiyama for his useful comments. H.Y. is supported by the Special Postdoctoral Researchers Program in RIKEN. A.B. is supported by JSPS Research Fellowship for Young Scientists.

References

Aharonian, F. A., & Atoyan, A. M. 1999, *A&A*, 351, 330
 Alves, D. R. 2004, *New Astronomy Review*, 48, 659
 Anders, E., & Grevesse, N. 1989, *Geochim. Cosmochim. Acta*, 53, 197
 Bamba, A., Ueno, M., Nakajima, H., & Koyama, K. 2004, *ApJ*, 602, 257
 Bamba, A., et al. 2008, *PASJ*, 60, S153

Cooper, R. L., Guerrero, M. A., Chu, Y.-H., Chen, C.-H. R., & Dunne, B. C. 2004, *ApJ*, 605, 751
 Dennerl, K., et al. 2001, *A&A*, 365, L202
 Dickey, J. M., & Lockman, F. J. 1990, *ARA&A*, 28, 215
 Dunne, B. C., Points, S. D., & Chu, Y.-H. 2001, *ApJS*, 136, 119
 Kalberla, P. M. W., et al. 2005, *A&A*, 440, 775
 Kennicutt, R. C., Jr., & Hodge, P. W. 1986, *ApJ*, 306, 130
 Koyama, K., Petre, R., Gotthelf, E. V., Hwang, U., Matsuura, M., Ozaki, M., & Holt, S. S. 1995, *Nature*, 378, 255
 Koyama, K., et al. 2007, *PASJ*, 59, S23
 Kushino, A., Ishisaki, Y., Morita, U., Yamasaki, N. Y., Ishida, M., Ohashi, T., & Ueda, Y. 2002, *PASJ*, 54, 327
 Long, K. S., Helfand, D. J., & Grabelsky, D. A. 1981, *ApJ*, 248, 925
 Lucke, P. B., & Hodge, P. W. 1970, *AJ*, 75, 171
 Mac Low, M.-M., & McCray, R. 1988, *ApJ*, 324, 776
 Masai, K. 1984, *Ap&SS*, 98, 367
 Mathewson, D. S., Ford, V. L., Tuohy, I. R., Mills, B. Y., Turtle, A. J., & Helfand, D. J. 1985, *ApJS*, 58, 197
 Mills, B. Y., Turtle, A. J., Little, A. G., & Durdin, J. M. 1984, *Australian Journal of Physics*, 37, 321
 Mitsuda, K., et al. 2007, *PASJ*, 59, S1
 Muno, M. P., Law, C., Clark, J. S., Dougherty, S. M., de Grijs, R., Portegies Zwart, S., & Yusef-Zadeh, F. 2006, *ApJ*, 650, 203
 Nakajima, H., et al. 2008, *PASJ*, 60, S1
 Reynolds, S. P. 1998, *ApJ*, 493, 375
 Russell, S. C., & Dopita, M. A. 1992, *ApJ*, 384, 508
 Serlemitsos, P. J., et al. 2007, *PASJ*, 59, S9
 Smith, R. K., Brickhouse, N. S., Liedahl, D. A., & Raymond, J. C. 2001, *ApJ*, 556, L91
 Takahashi, T., et al. 2008, *PASJ*, 60, S131
 Tawa, N., et al. 2008, *PASJ*, 60, S11
 Vink, J., Bleeker, J., van der Heyden, K., Bykov, A., Bamba, A., & Yamazaki, R. 2006, *ApJ*, 648, L33
 Wolk, S. J., Bourke, T. L., Smith, R. K., Spitzbart, B., & Alves, J. 2002, *ApJL*, 580, L1
 Yamaguchi, H., Koyama, K., Nakajima, H., Bamba, A., Yamazaki, R., Vink, J., & Kawachi, A. 2008, *PASJ*, 60, S123
 Yamaguchi, R., Mizuno, N., Onishi, T., Mizuno, A., & Fukui, Y. 2001, *PASJ*, 53, 959